Journal of Materials Chemistry C

ROYAL SOCIETY OF CHEMISTRY

PAPER

View Article Online
View Journal | View Issue

Cite this: J. Mater. Chem. C, 2025, 13, 6605

Multilevel carbon composite construction of NASICON-type $NaVPO_4F$/C/CNT cathode material for enhanced-performance sodium-ion batteries†

Kang Tang,[a] Hualing Tian,[a] Yanhui Zhang,[a] Yanjun Cai,[a] Hong Du,[a] Mofan Zhu,[a] Xiang Yao*[a] and Zhi Su*[ab]

Received 8th November 2024,
Accepted 31st January 2025

DOI: 10.1039/d4tc04746j

rsc.li/materials-c

$NaVPO_4F$ (NVPF) holds significant promise for advancing the commercialization of sodium-ion batteries owing to its high voltage of 3.4 V, impressive theoretical capacity of 143 mA h g^{-1}, and low vanadium content. However, its further development is hindered by its limited internal electronic conductivity. To address this issue, herein, an additional network of highly conductive carbon nanotube (CNT) was applied onto a layer of reduced carbon to form a multilevel carbon structure. The introduction of 3D tubular network increased the specific surface area of the material, inhibited the growth of the particle size of the sample, and accelerated the transport of sodium ions, which provided a stabilizing barrier to mitigate structural degradation. The prepared $NaVPO_4F$/C/CNT10% (NVPF/C/CNT10%) cathode demonstrated a discharge specific capacity of 125.6 mA h g^{-1} at 0.2C, achieving impressive capacity retention of 98.4% after 100 cycles. Furthermore, after 1000 cycles at 5C, it exhibited the capacity retention of 78%. Notably, the fabricated full battery demonstrated an exceptionally high capacity retention of 86.2% after 300 cycles at the same rate. Through *ex situ* XRD and XPS analyses of the NVPF/C/CNT10% sample, the mechanism of sodium-ion intercalation/deintercalation was disclosed during the charging/discharging processes. This study paves the way for the development of highperformance cathode materials for sodium-ion batteries.

1. Introduction

The growing demand for lithium-ion batteries (LIBs) has inevitably brought to light the limitations of global lithium resources, leading to a continuous rise in their prices and impeding their widespread implementation in future developments.[1] Compared to lithium reserves of 0.0065%, the total sodium content in Earth's crust is about 2.7%, making it a more abundant resource with lower extraction costs.[2] Furthermore, both sodium and lithium belong to the same main group and exhibit similar electrochemical mechanisms, indicating that sodium-ion batteries (SIBs) hold great potential as next-generation large-scale energy storage systems.[3] In SIBs, the primary role of the cathode material is to supply sodium ions, implying that it can exhibit a robust sodium-ion storage capacity as well as a high desodiation potential.[4] To date, the most promising cathode materials have predominantly been categorized into polyanion compounds,[5,6] transition metal oxides,[7,8] and Prussian blue analogues.[9–11]

Among various materials, the polyanionic phosphate compound $NaVPO_4F$ (NVPF) is distinguished by its unique structure, wherein its P–O tetrahedra are interconnected with V–O–F octahedra through shared oxygen atoms, resulting in a stable three-dimensional framework.[12–14] The F atom acts as a potent electron-withdrawing group, effectively diminishing the electron density surrounding the V–O octahedra and consequently enhancing the redox potential of vanadium.[15,16] With notable advantages such as a high operating voltage of 3.4 V, an impressive theoretical capacity of 143 mA h g^{-1}, low toxicity associated with V, and significant application potential, NVPF has emerged as a promising cathode material. However, its limited electronic conductivity poses challenges to its further development.[17] A variety of approaches have been employed to address this issue, including the manipulation of microscopic morphology,[18–20] element doping,[21–23] electrode design,[24] and surface coating.[25,26] Among these strategies, applying a highly conductive material as a surface coating represents the most straightforward and effective method for enhancing the conductivity of the sample. Zhang *et al.* developed $Na_3V_2(PO_4)_2F_3$@RuO_2 through the deposition of a highly conductive metal

[a] College of Chemistry and Chemical Engineering, Xinjiang Key Laboratory of Energy Storage and Photoelectroctalytic Materials, Xinjiang Normal University, Urumqi 830054, Xinjiang, P. R. China. E-mail: yaoxiangxjnu@163.com, suzhixj@163.com

[b] Xinjiang University, Urumqi, 830046, Xinjiang, P. R. China

† Electronic supplementary information (ESI) available: https://doi.org/10.1039/d4tc04746j

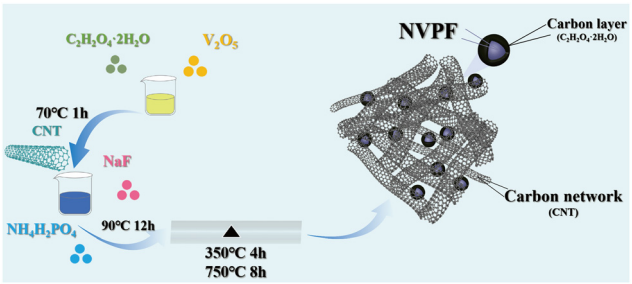

Fig. 1 Preparation process of NVPF/C/CNT with a multilevel carbon network.

oxide RuO_2, which facilitated a substantial enhancement in the material electrical conductivity and electrochemical performance.[27] Zhang *et al.* demonstrated that $Na_4MnV(PO_4)_3$/NC@CNTs exhibited a remarkable capacity retention of 77.5% at a discharge rate of 10C after 1500 cycles, which can be attributed to the N-doped double carbon layer, thus effectively enhancing both the electrical conductivity and stability of the material.[28]

Herein, we constructed a $NaVPO_4F$/C/CNTx (x = 0, 5%, 10% and 15%, hereafter referred to as NVPF/C and NVPF/C/CNTx) composite by applying a highly conductive CNT network onto the surface of the single carbon layer. Experimental results demonstrated that in comparison to the single carbon structure, the multilevel carbon architecture significantly accelerated Na^+ transport and effectively enhanced the structural stability. NVPF/C/CNT10% demonstrated a remarkable reversible discharge capacity of 125.6 mA h g^{-1} at 0.2C, with a capacity retention of 98.4% after 100 cycles. Notably, the assembled full battery exhibits an impressive capacity retention of 86.2% after 300 cycles at 5C. The sodium storage mechanism was further elucidated through *ex situ* XRD and XPS analyses conducted at various voltage levels.

2. Results and discussion

2.1. Morphology and structural characteristics

As depicted in Fig. 1, the preparation process for NVPF/C/CNT samples involves a sol–gel method, followed by a high-temperature calcination. V_2O_5 is reduced to V^{3+} using a slight excess of oxalic acid, with the remaining acid forming the first carbon layer during the high-temperature calcination. Subsequently, $NH_4H_2PO_4$, NaF, and CNT were added. CNT, serving as the second carbon network, created a three-dimensional conductive network on NVPF/C during the calcination, culminating in the formation of NVPF/C/CNT.

The XRD patterns of the NVPF/C and NVPF/C/CNT series samples are presented in Fig. 2a. All observed diffraction peaks correspond well to the monoclinic crystal structure of NVPF, which belongs to the $C2/c$ space group. This observation is consistent with previously reported findings.[29,30] The XRD peak profiles for the samples containing 5%, 10%, and 15% CNT were largely similar, suggesting that the incorporation of CNT does not adversely affect the crystallization process of NVPF. Fig. 2b illustrates the TG curves of the materials evaluated in air, revealing that the carbon contents of NVPF/C and

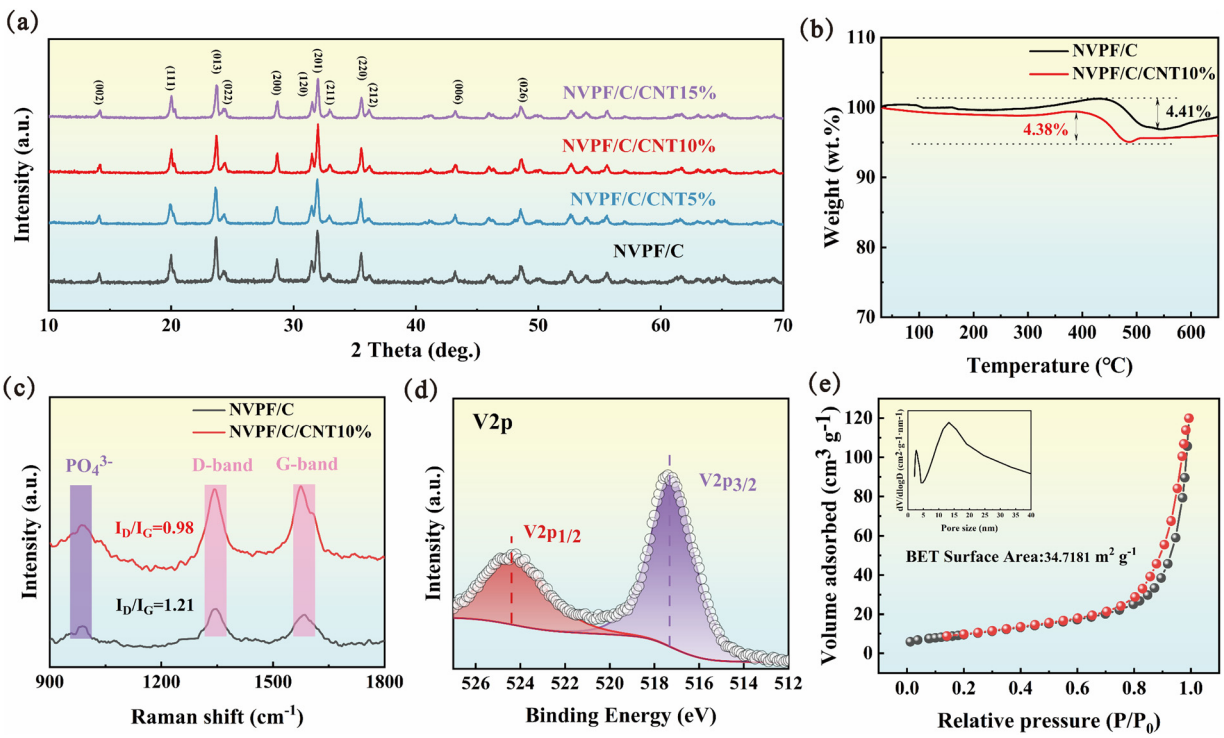

Fig. 2 (a) XRD patterns of the four samples; (b) TG curves and (c) Raman spectra of NVPF/C and NVPF/C/CNT10% samples; (d) XPS V 2p spectrum and (e) BET/BJH curve of NVPF/C/CNT10% sample.

NVPF/C/CNT10% are 4.41% and 4.38%, respectively. The carbon contents among the samples are similar, which is in line with the results of the experimental design.

Raman spectroscopy was employed to further investigate the carbon species in the NVPF/C and NVPF/C/CNT10% samples, as illustrated in Fig. 2c. Both samples exhibit distinct peaks at approximately 1000, 1350, and 1600 cm^{-1}, which correspond to the stretching vibration of PO_4^{3-}, the D peak (defect induced) of carbon, and the G peak (crystalline graphite) of carbon, respectively. The intensity ratio of the D peak and the G peak (I_D/I_G) serves as an indicator of the sample's degree of graphitization.[31] Notably, the I_D/I_G value for NVPF/C/CNT10% (0.98) is significantly lower than that for NVPF/C (1.21), suggesting that CNT incorporation enhances graphitization and subsequently improves electrical conductivity. The elemental makeup and oxidation state of the NVPF/C/CNT10% sample were analyzed using XPS, as indicated by the comprehensive spectrum analysis (Fig. S1, ESI†), which identified the elements Na, V, P, O, F, and C. The high-resolution C 1s spectrum was fitted to show the presence of C–C, C–O, and C═O bonds. In the V 2p spectrum shown in Fig. 2d, two peaks are observed at binding energy values of 517.1 eV and 524.2 eV, which correspond to the V $2p_{3/2}$ and V $2p_{1/2}$ orbitals, respectively, indicating presence of trivalent vanadium.[32] Meanwhile, BET analysis reveals that the specific surface area of the multilevel carbon structure in NVPF/C/CNT (34.7181 $m^2\ g^{-1}$) is significantly greater than that of NVPF/C (4.1728 $m^2\ g^{-1}$). This enhanced specific surface area facilitates an increased wettability between the electrode and the electrolyte (Fig. 2e and Fig. S3, ESI†).

The microscopic morphology of the sample was examined using SEM and TEM to investigate the effects of the multilevel carbon composite structure. As shown in Fig. 3(a–d) and Fig. S4 (ESI†), the surface of the NVPF/C sample displays larger particle sizes, with an average diameter of approximately 3.55 μm. In contrast, the average particle diameters for the NVPF/C/CNT5%, NVPF/C/CNT10%, and NVPF/C/CNT15% concentrations are measured at 2.69, 2.12, and 1.63 μm, respectively. The surface of the NVPF/C/CNT10% sample is intricately enveloped by a three-dimensional tubular network formed by CNT, which not only increases electron transport rates but also effectively curtails the growth of NVPF particles, thereby augmenting its electrochemical performance. The TEM images of the NVPF/C/CNT10% sample presented in Fig. 3e and f distinctly illustrate that CNT is uniformly enveloping on the surface of the sample. In Fig. 3g and Fig. S5 (ESI†), a carbon layer of approximately 3 nm thick is clearly discernible on the surface of the NVPF sample, resulting from the thermal decomposition of oxalic acid. Beyond this carbon layer, CNTs can be tightly wrapped around the sample's surface, corroborating the findings from SEM. Additionally, measurements reveal an interplanar spacing of 0.281 nm for the sample, which corresponds to the (120) plane of NVPF.[33] Furthermore, the mapping images of the NVPF/C/CNT10% sample are presented in Fig. 3h, illustrating a uniform distribution of elements C, Na, V, P, O, and F throughout the sample.

2.2. Electrochemical evaluation of NVPF/C/CNT in half cells

To explore the influence of a multilevel carbon structure on the sodium storage performance of NVPF cathode material,

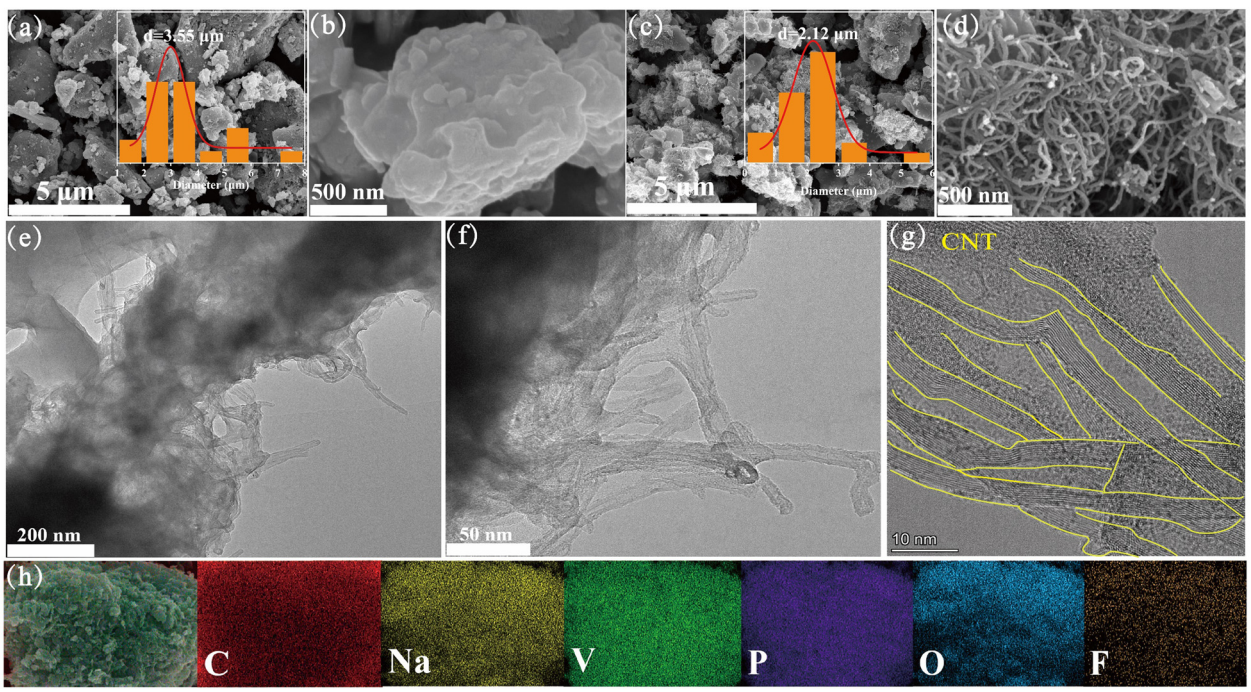

Fig. 3 SEM images of (a) and (b) NVPF/C; (c) and (d) NVPF/C/CNT10%; (e)–(g) TEM and HRTEM images of NVPF/C/CNT10%; (h) elemental mapping images of NVPF/C/CNT10%.

electrochemical tests were performed using CR2032-type half cells within a voltage range of 2.5–4.0 V. Fig. 4a illustrates the galvanostatic charge–discharge (GCD) curves for all samples at 0.2C. A pair of charging and discharging plateaux are observed at about 3.4 V, which correspond to the redox reaction between V^{3+} and V^{4+}. The charging curves exhibit smooth transitions, and the discharging curves reveal a distinct step-like platform phenomenon, this behavior is attributed to the formation of an *in situ* passivation layer on the surface of the sodium counter electrode due to interactions withsolvent in the electrolyte.[34,35] This passivation layer forms during discharge and dissipates upon charging, recurring consistently throughout cycling. The initial specific capacities of NVPF/C, NVPF/C/CNT5%, NVPF/C/CNT10%, and NVPF/C/CNT15% were measured to be 109.4, 121.9, 125.6, and 111.3 mA h g^{-1}, respectively. In particular, NVPF/C/CNT10% exhibited the highest initial specific capacity among these samples. After 100 cycles, it retained a capacity of 123.7 mA h g^{-1} with a retention of 98.4%. In contrast, the capacity retention for NVPF/C was recorded at only 87.8% (Fig. 4b). The rate performance of the four samples is illustrated in Fig. 4c. At 1C, NVPF/C/CNT10% demonstrates a specific capacity of 113.8 mA h g^{-1}, surpassing that of NVPF/C (99.4 mA h g^{-1}), NVPF/CNT5% (107.4 mA h g^{-1}), and NVPF/CNT15% (106.2 mA h g^{-1}). Additionally, at varying rates of 2, 3, 5, and 10C, the specific capacities for NVPF/C/CNT10% were recorded as 111.1, 108.7, 104.9, and 100.1 mA h g^{-1}, respectively, these values are significantly higher than those for NVPF/C (92.5, 85.5, 75.6, and 57.3 mA h g^{-1}). A comparison of the discharge curves for both NVPF/C and NVPF/C/CNT10% across different rates reveals that the curve for NVPF/C/CNT10% exhibits minimal polarization and maintains a more stable voltage platform (Fig. S6, ESI†).

In order to comprehensively assess the long-term cycling stability of the cathode material, the results from 1000 cycles were obtained at 5C in Fig. 4d. The initial discharge specific capacity of NVPF/C/CNT10% at this rate was measured at 107.7 mA h g^{-1}, and after completing 1000 cycles, it retained a capacity of 84 mA h g^{-1}, corresponding to the retention of 78%. In comparison, the capacity retention for NVPF/C/CNT5% and NVPF/C/CNT15% was found to be 72.8% and 71.6%, respectively. Conversely, NVPF/C exhibited poor performance under high rates, its specific capacity experienced a pronounced decline throughout the cycling process, culminating in final retention of merely 11.5%. Following disassembly of the NVPF/C/CNT10% electrode post-1000 cycles at 5C, XRD and SEM analyses were performed, as illustrated in Fig. S6 and S7 (ESI†). The diffraction peaks for NVPF/C/CNT10% displayed no significant alterations in either position or intensity. Additionally, SEM analysis indicates that the multilevel carbon architecture significantly alleviates the effects of high-intensity current on the sample, thereby preserving the integrity of its surface. These results show that the multilevel carbon architecture effectively enhances structural stability while facilitating commendable electrochemical performance. Fig. 4e presents a comparison of NVPF/C/CNT10% with previously reported materials, demonstrating that NVPF/C/CNT10% exhibits outstanding overall performance (Table S1, ESI†).

The influence of multilevel carbon on the reaction kinetics of the NVPF cathode material was investigated through CV tests conducted on the four materials at a scanning rate of 0.1 mV s^{-1}, as shown in Fig. 5a. All CV curves display a pair of

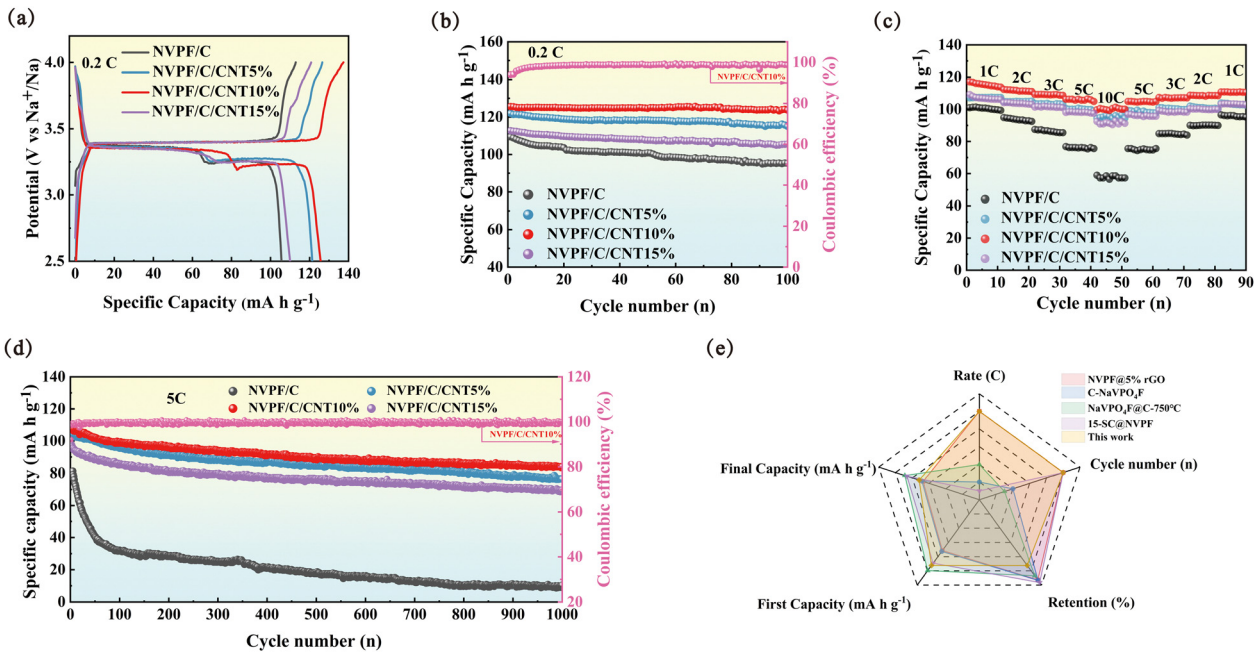

Fig. 4 (a) Initial GCD curves; (b) cycling performance at 0.2C; (c) rate performance; and (d) 5C long cycling stability of the four samples; (e) performance comparison chart of the NVPF/C/CNT10% sample with other reported materials.

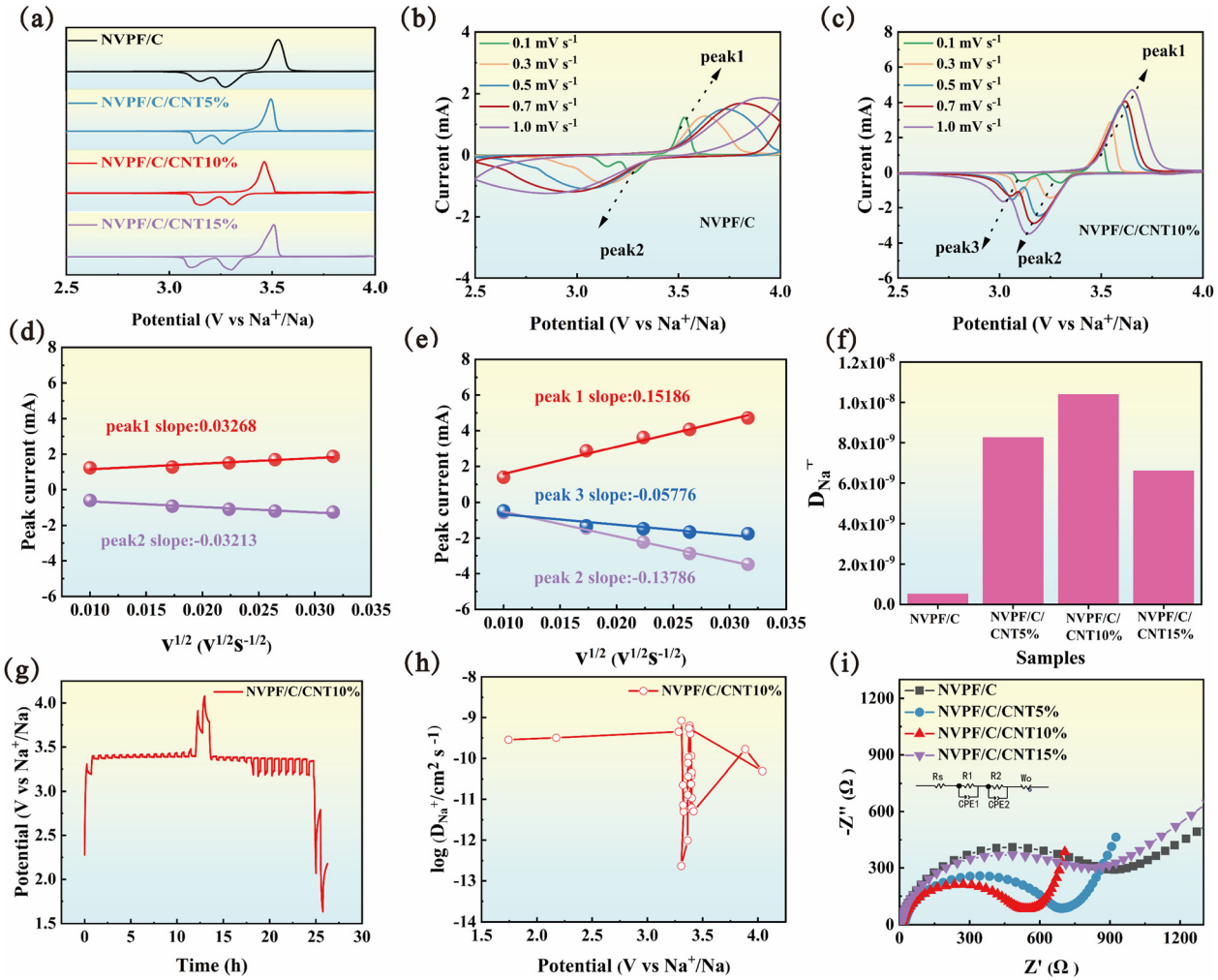

Fig. 5 (a) CV plots of NVPF/C/CNT at 0.1 mV s^{-1} within 2.5–4.0 V; CV curves obtained at various scanning rates for (b) NVPF/C and (c) NVPF/C/CNT10%; linear fitting graph of i_p and $v^{1/2}$ based on different sweep speeds for (d) NVPF/C and (e) NVPF/C/CNT10%; (f) corresponding Na^+ diffusion coefficient; (g) voltage profile during GITT for NVPF/C/C; (h) the apparent diffusion coefficients of Na^+ were calculated from the GITT profiles; (i) four samples of the Nyquist plot.

oxidation–reduction peaks at about 3.4 V, corresponding to the V^{3+}/V^{4+} redox couple, which aligns with the discharge–charge curve plateau observed in the half-cell configuration. Interestingly, the reduction peak near 3.2 V bifurcates into two distinct peaks from an initial single peak, this phenomenon may be attributed to localized temperature increases during charging and discharging processes, which facilitates Na^+ migration from the Na(1) site to the Na(2) site.[36,37] Furthermore, NVPF/C/CNT10% demonstrates a reduced polarization value between its oxidation and reduction peaks, thereby enhancing rapid Na^+ de-intercalation. Fig. 5(b and c) and Fig. S8 (ESI†) illustrate the CV curves of the four cathode materials at varying scan rates ranging from 0.1 to 1 mV s^{-1}. When the scan rate increases, the intensity of the redox peaks enhances progressively. NVPF/C exhibits broad and weak characteristic peaks with minimum overlap between them. In contrast, NVPF/C/CNT10% displays a distinct and sharp characteristic peak characterized by significant overlap, indicating superior reversibility. The linear relationship between peak current (i_p) and scan rate ($v^{1/2}$) for both NVPF/C and NVPF/C/CNT10% is depicted in Fig. 5(d and e), while the apparent diffusion coefficients of D_{Na^+} were calculated using eq (1.1) for each material.

$$i_p = 2.69 \times 10^5 n^{3/2} A D^{1/2} C v^{1/2} \quad (1.1)$$

In the equation, i_p represents the peak current density, n denotes the number of electron transfers per reactant molecule in the redox reaction (for NVPF, n = 1), A signifies the electrode's surface area, C indicates the concentration of Na^+ within the crystal lattice, and v refers to the sweep rate.

The results presented in Fig. 5(f) reveal that D_{Na^+} values for NVPF/C, NVPF/C/CNT5%, NVPF/C/CNT10%, and NVPF/C/CNT15% were quantified as 5.22×10^{-10}, 8.27×10^{-9}, 1.03×10^{-8}, and 6.60×10^{-9}, respectively. This indicates that the conductive network established through multilevel carbon coating facilitates a more rapid transport speed of Na^+ compared to that observed in NVPF/C. Further comparison of the Na^+ diffusion coefficients for NVPF/C and NVPF/C/CNT10% using GITT, as illustrated in Fig. 5(g and h), it reveals that both

voltage–time curves exhibit a similar trend, with a distinct plateau observed at about 3.4 V, aligning well with the CV results. Calculations based on eq (S1.2, ESI†) indicate that the D_{Na^+} of NVPF/C/CNT10% ($10^{-9.07}$–$10^{-12.6}$) significantly outperforms that of NVPF/C ($10^{-9.23}$–$10^{-13.2}$) (Fig. S9, ESI†). Additionally, EIS further corroborates the superior Na^+ transport dynamics of NVPF/C/CNT10%, as depicted in Fig. 5i. The charge transfer resistance for NVPF/C/CNT10% is measured at 531.2 Ω, markedly lower than that of NVPF/C at 1045.1 Ω.

To further elucidate the sodium storage mechanism of NVPF/C/CNT10%, *ex situ* XRD and XPS analyses were performed under various conditions. The results illustrated in Fig. 6(a and b) reveal characteristic diffraction peaks at 23.72°, 24.35°, and 28.66°, corresponding to the (013), (022), and (200) planes, respectively. Upon charging to 3.4 V, a pronounced shift of all diffraction peaks towards higher angles was observed, which is attributed to the extraction of Na^+ ($NaVPO_4F \rightarrow Na_{1-x}VPO_4F + xNa^+ + xe^-$), resulting in a contraction of the crystal lattice and an oxidation–reduction transition from trivalent to tetravalent vanadium. At the maximum voltage of 4 V, no significant alterations in the peak positions were detected, implying that no additional reactions occurred at this stage. During subsequent discharge cycles, the diffraction peaks gradually reverted to their original positions ($2\theta_{(013)} = 23.68°$, $2\theta_{(022)} = 24.44°$, $2\theta_{(200)} = 28.60°$). These findings demonstrate that NVPF/C/CNT10% maintains a stable crystal structure throughout both charging and discharging processes, thereby confirming the sample's exceptional structural stability. Fig. 6c shows the XPS spectra of V under varying voltage states. When the voltage rises to 4 V, the $2p_{1/2}$ (524.11 eV) and $2p_{3/2}$ (516.95 eV) orbitals of V^{3+} exhibit a shift towards higher binding energies, ultimately corresponding to the $2p_{1/2}$ (524.80 eV) and $2p_{3/2}$ (517.82 eV) orbitals of V^{4+}, respectively, which suggests Na^+ removal during the transition from $V^{3+} - e^- \rightarrow V^{4+}$. When the voltage returns to 2.5 V, the 2p orbitals revert to those characteristic of V^{3+} with Na^+ insertion conversion of $V^{4+} + e^- \rightarrow V^{3+}$, the $2p_{1/2}$ is at 524.15 eV and the $2p_{3/2}$ is at 517.22 eV. The findings from XPS are in agreement with CV and *ex situ* XRD results.

2.3. Electrochemical evaluation of HC//NVPF/C/CNT10% in full battery

The full battery configuration of HC//NVPF/C/CNT10% was established by integrating a hard carbon (HC) anode with the NVPF/C/CNT10% cathode, as illustrated in Fig. 7a. The GCD

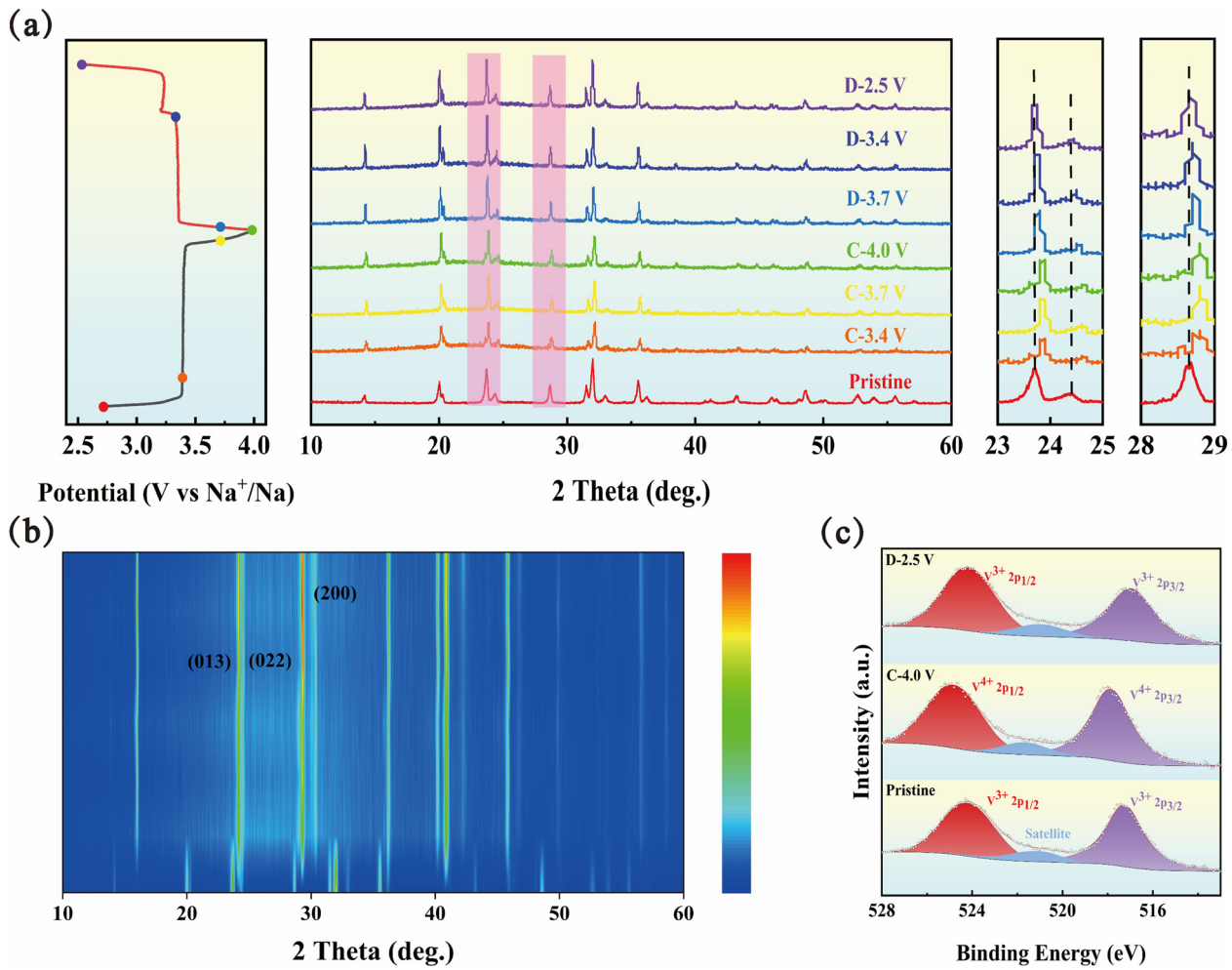

Fig. 6 (a) XRD patterns of NVPF/C/CNT10% electrodes under different states; (b) *ex situ* XRD contour plot of NVPF/C/CNT10%; (c) XPS spectra of V at different voltages.

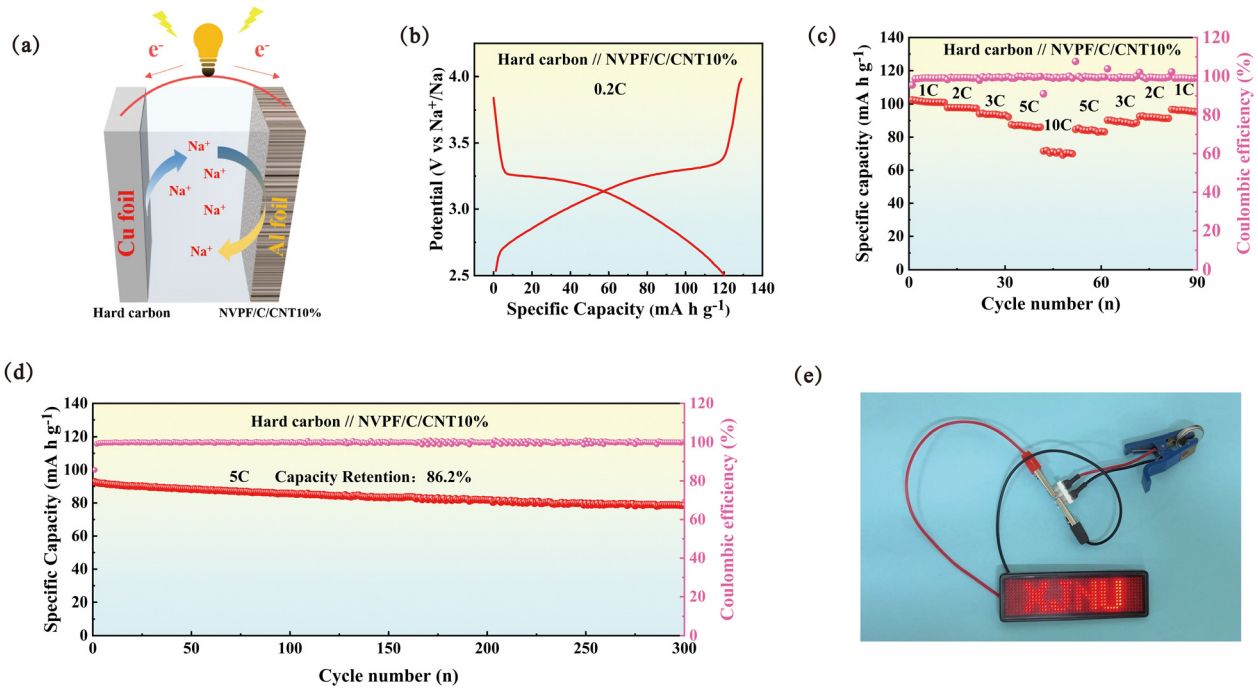

Fig. 7 (a) Schematic diagram of the HC//NVPF/C/CNT10% full battery; (b) GCD curves at 0.2C; (c) rate capabilities from 1C to 10C; (d) cycling performance; (e) digital photographs of LED bulbs powered by a full battery.

curve for HC//NVPF/C/CNT10% is presented in Fig. 7b, displaying a discharge specific capacity of 118.2 mA h g^{-1} at 0.2C. Furthermore, the discharge specific capacities of HC//NVPF/C/CNT10% at various current rates of 1, 2, 3, 5, and 10C were measured to be 100.9, 97.4, 93.8, 86.8, and 71.1 mA h g^{-1}, respectively (Fig. 7c). At 5C, the discharge specific capacity of HC//NVPF/C/CNT10% was measured at 92.7 mA h g^{-1}, with capacity retention of 86.2% after 300 cycles (Fig. 7d). The aforementioned results suggest that NVPF/C/CNT10% exhibits commendable electrochemical performance in the full battery system. At the same time, Fig. 7f shows that the HC//NVPF/C/CNT10% full battery lights up the LED bulb, indicating that the NVPF/C/CNT10% cathode material has great practical application value.

Conclusions

In summary, multilevel carbon composite NVPF/C/CNT (5%, 10%, and 15%) cathode materials were successfully prepared using the sol–gel method. Among these materials, NVPF/C/CNT10% demonstrates superior electrochemical performance due to the formation of conductive networks that facilitates Na^+ transport. The discharge specific capacity is 125.6 mA h g^{-1} at 0.2C, with the capacity retention of 98.4% after 100 cycles. Furthermore, after 1000 cycles at 5C, the capacity retention of 78% was observed. SEM and XRD analyses conducted before and after cycling reveal that the three-dimensional tubular network established by the multilevel carbon structure effectively mitigates high current impacts, thereby enhancing material stability. Additionally, the assembled full battery HC//NVPF/C/CNT10% maintains the capacity retention of 86.2% after 300 cycles at 5C, demonstrating significant practical value. *Ex situ* XRD and XPS tests performed under varying voltages states elucidate the solid-solution phase conversion mechanism occurring in NVPF/C/CNT10% during charge–discharge processes. This research paves new avenues for advancing commercialization of NASICON-type polyanion cathode materials.

Author contributions

Kang Tang: writing – review & editing, writing – original draft, data curation. Hualing Tian: investigation. Yanhui Zhang: software. Yanjun Cai: supervision, conceptualization. Hong Du: validation. Mofan Zhu: data analysis. Xiang Yao: writing – review & editing. Zhi Su: project administration, funding acquisition.

Data availability

The data are available from the corresponding author on reasonable request.

Conflicts of interest

The authors declare that they have no known competing financial interests or personal relationships that could have appeared to influence the work reported in this paper.

Acknowledgements

This study was sponsored by Natural Science Foundation of Xinjiang Uygur Autonomous Region (2022D01B37), Doctoral Research Foundation of Xinjiang Normal University (XJNUBS2309), College Student Innovation and Entrepreneurship Training Program Project of Xinjiang Normal University (S202410762007), National Natural Science Foundation of China (22169020), and Xinjiang Key Research and Development Project (2021B01001-1, 2022B01023-2).

Notes and references

1 L. Ji, Z. Lin, M. Alcoutlabi and X. Zhang, Recent developments in nanostructured anode materials for rechargeable lithium-ion batteries, *Energy Environ. Sci.*, 2011, **4**, 2682–2699.

2 E. Goikolea, V. Palomares, S. Wang, I. R. de Larramendi, X. Guo, G. Wang and T. Rojo, Na-Ion Batteries---Approaching Old and New Challenges, *Adv. Energy Mater.*, 2020, **10**, 2002055.

3 X. X. Zeng, Y. T. Xu, Y. X. Yin, X. W. Wu, J. Yue and Y. G. Guo, Recent advances in nanostructured electrode-electrolyte design for safe and next-generation electrochemical energy storage, *Mater. Today Nano*, 2019, **8**, 100057.

4 R. Usiskin, Y. Lu, J. Popovic, M. Law, P. Balaya, Y. Hu and J. Maier, Fundamentals, status and promise of sodium-based batteries, *Nat. Rev. Mater.*, 2021, **6**, 1020–1035.

5 J. Zeng, J. Gao, W. Jian, H. Wang, W. Li, N. Hong, B. Zhang, J. Huang, B. Song, C. Gan, S. Yasar, W. Deng, G. Zou, H. Hou and X. Ji, Multivalent Cation Incorporated into Manganese-Iron Based NASICON Cathodes for High Voltage Sodium-Ion Batteries, *Adv. Funct. Mater.*, 2024, 2410992.

6 J. Guo, H. Zhang, Z. Gu, M. Du, H. Lü, X. Zhao, J. Yang, W. Li, S. Kang, W. Zou and X. Wu, Heterogeneous NASICON-Type Composite as Low-Cost, High-Performance Cathode for Sodium-Ion Batteries, *Adv. Funct. Mater.*, 2022, **32**, 2209482.

7 Q. Liu, Z. Hu, M. Chen, C. Zou, H. Jin, S. Wang, S. Chou and S. Dou, Recent Progress of Layered Transition Metal Oxide Cathodes for Sodium-Ion Batteries, *Small*, 2019, **15**, 1805381.

8 P. Wang, Y. You, Y. Yin and Y. Guo, Layered Oxide Cathodes for Sodium-Ion Batteries: Phase Transition, Air Stability, and Performance, *Adv. Energy Mater.*, 2018, **8**, 1701912.

9 J. Peng, W. Zhang, Q. Liu, J. Wang, S. Chou, H. Liu and S. Dou, Prussian Blue Analogues for Sodium-Ion Batteries: Past, Present, and Future, *Adv. Mater.*, 2022, **34**, 2108384.

10 L. Wang, J. Song, R. Qiao, L. A. Wray, M. A. Hossain, Y. Chuang, W. Yang, Y. Lu, D. Evans, J. Lee, S. Vail, X. Zhao, M. Nishijima, S. Kakimoto and J. B. Goodenough, Rhombohedral Prussian White as Cathode for Rechargeable Sodium-Ion Batteries, *J. Am. Chem. Soc.*, 2015, **137**, 2548–2554.

11 B. Xie, B. Sun, T. Gao, Y. Ma, G. Yin and P. Zuo, Recent progress of Prussian blue analogues as cathode materials for nonaqueous sodium-ion batteries, *Coord. Chem. Rev.*, 2022, **460**, 214478.

12 X. Shen, Q. Zhou, M. Han, X. Qi, B. Li, Q. Zhang, J. Zhao, C. Yang, H. Liu and Y. Hu, Rapid mechanochemical synthesis of polyanionic cathode with improved electrochemical performance for Na-ion batteries, *Nat. Commun.*, 2021, **12**, 2848.

13 L. Xiao, F. Ji, J. Zhang, X. Chen and Y. Fang, Doping Regulation in Polyanionic Compounds for Advanced Sodium-Ion Batteries, *Small*, 2023, **19**, 2205732.

14 Z. Lv, M. Ling, M. Yue, X. Li, M. Song, Q. Zheng and H. Zhang, Vanadium-based polyanionic compounds as cathode materials for sodium-ion batteries: Toward high-energy and high-power applications, *J. Energy Chem.*, 2021, **55**, 361–390.

15 S. D. Shraer, N. D. Luchinin, I. A. Trussov, D. A. Aksyonov, A. V. Morozov, S. V. Ryazantsev, A. R. Iarchuk, P. A. Morozova, V. A. Nikitina, K. J. Stevenson, E. V. Antipov, A. M. Abakumov and S. S. Fedotov, Development of vanadium-based polyanion positive electrode active materials for high-voltage sodium-based batteries, *Nat. Commun.*, 2022, **13**, 4097.

16 L. Deng, F. Yu, Y. Xia, Y. Jiang, X. Sui, L. Zhao, X. Meng, L. Que and Z. Wang, Stabilizing fluorine to achieve high-voltage and ultra-stable $Na_3V_2(PO_4)_2F_3$ cathode for sodium ion batteries, *Nano Energy*, 2021, **82**, 105659.

17 Y. Zuo, J. Yue, Z. Ma and Z. Zuo, Facile fabrication of carbon-encapsulated $NaVPO_4F$ nanocomposite as a high-rate and long-cycle life cathode material for sodium energy storage, *J. Phys. Chem. Solids*, 2022, **160**, 110354.

18 H. Chen, Y. Yang, R. Nie, C. Li, S. Xu, M. Zhou, X. Zhang and H. Zhou, Micro-nano $Na_3V_2(PO_4)_3$/C derived from metal-organic frameworks for high performance sodium ion batteries, *J. Alloys Compd.*, 2023, **932**, 167695.

19 K. Liang, S. Wang, H. Zhao, X. Huang, Y. Ren, Z. He, J. Mao and J. Zheng, A facile strategy for developing uniform hierarchical $Na_3V_2(PO_4)_2F_3$@carbonized polyacrylonitrile multi-clustered hollow microspheres for high-energy-density sodium-ion batteries, *Chem. Eng. J.*, 2022, **428**, 131780.

20 Z. Hu, R. Zhang, C. Fan, X. Liu, P. Gao, W. Zhang, Z. Liu, S. Han, J. Liu and J. Liu, Synergistic Effect, Structural and Morphology Evolution, and Doping Mechanism of Spherical Br-Doped $Na_3V_2(PO_4)_2F_3$/C toward Enhanced Sodium Storage, *Small*, 2022, **18**, 2201719.

21 S. Sun, Y. Chen, Q. Bai, Q. Huang, C. Liu, S. He, Y. Yang, Y. Wang and L. Guo, Unraveling the modified regulation of ternary substitution on $Na_3V_2(PO_4)_3$ for sodium ion batteries, *J. Mater. Chem. A*, 2022, **10**, 11340–11353.

22 Z. Tian, Y. Chen, S. Sun, X. Jiang, H. Liu, C. Wang, Q. Huang, C. Liu, Y. Wang and L. Guo, Activating the Extra Redox Couple of Co^{2+}/Co^{3+} for a Synergistic K/Co Co-Substituted and Carbon Nanotube-Enwrapped $Na_3V_2(PO_4)_3$ Cathode with a Superior Sodium Storage Property, *ACS Appl. Mater. Interfaces*, 2022, **14**, 611–621.

23 J. Zhao, W. Yan, S. Li, S. Li, W. Wang and Y. Bai, Double-pinning effect assisting $Na_4VMn(PO_4)_3$ with superior

structural and electrochemical stabilization for sodium-ion batteries, *Nano Energy*, 2024, **119**, 109002.
24 Y. Liu, X. Wu, A. Moeez, Z. Peng, Y. Xia, D. Zhao, J. Liu and W. Li, Na-Rich $Na_3V_2(PO_4)_3$ Cathodes for Long Cycling Rechargeable Sodium Full Cells, *Adv. Energy Mater.*, 2023, **13**, 2203283.
25 D. Ma, L. Zhang, T. Li, C. Liu, G. Liang, Y. Zhou and X. Yang, Enhanced electrochemical performance of carbon and aluminum oxide co-coated $Na_3V_2(PO_4)_2F_3$ cathode material for sodium ion batteries, *Electrochim. Acta*, 2018, **283**, 1441–1449.
26 J. Wang, L. Zhao and F. Lu, Hierarchical cathode constructed by carbon coated $Na_{3.5}VMn_{0.5}Cr_{0.5}(PO_4)_3$ nanoparticles on rGO for high-capacity and long-cycle life sodium storage, *Mater. Adv.*, 2023, **4**, 1998–2007.
27 Y. Zhang, J. Xun, K. Zhang, B. Zhang and H. Xu, 2D-lamellar stacked $Na_3V_2(PO_4)_2F_3$@RuO_2 as a high-voltage, high-rate capability and long-term cycling cathode material for sodium ion batteries, *J. Mater. Chem. A*, 2022, **10**, 11163–11171.
28 W. Zhang, Z. Zhang, H. Li, D. Wang, T. Wang, X. Sun, J. Zheng and Y. Lai, Engineering 3D Well-Interconnected $Na_4MnV(PO_4)_3$ Facilitates Ultrafast and Ultrastable Sodium Storage, *ACS Appl. Mater. Interfaces*, 2019, **11**, 35746–35754.
29 B. Cheng, S. Zhang, F. Zou, L. Luo, Y. Chen, S. Chen, H. Zhuo and X. Zeng, Nano-$NaVPO_4F$ enwrapped in reduced graphene oxide as a cathode material for long-cycle and high-rate sodium-ion batteries, *J. Alloys Compd.*, 2019, **811**, 151828.
30 V. K. Kumar, S. Ghosh, S. Biswas and S. K. Martha, Pitch-Derived Soft-Carbon-Wrapped $NaVPO_4F$ Composite as a Potential Cathode Material for Sodium-Ion Batteries, *ACS Appl. Energy Mater.*, 2021, **4**, 4059–4069.
31 S. Wang, J. Zheng, L. He, L. Zhang, X. Ge, S. Li, X. Wang and Z. Zhang, Carbon-Modified NASICON $Na_4FeV(PO_4)_3$ Cathode with Enhanced Kinetics for High-Performance Sodium-Ion Batteries, *ACS Appl. Energy Mater.*, 2022, **5**, 9616–9624.
32 Y. Zhou, G. Xu, J. Lin, J. Zhu, J. Pan, G. Fang, S. Liang and X. Cao, A multicationic-substituted configurational entropy-enabled NASICON cathode for high-power sodium-ion batteries, *Nano Energy*, 2024, **128**, 109812.
33 M. Ling, F. Li, H. Yi, X. Li, G. Hou, Q. Zheng and H. Zhang, Superior Na-storage performance of molten-state-blending-synthesized monoclinic $NaVPO_4F$ nanoplates for Na-ion batteries, *J. Mater. Chem. A*, 2018, **6**, 24201–24209.
34 M. Law and P. Balaya, $NaVPO_4F$ with high cycling stability as a promising cathode for sodium-ion battery, *Energy Storage Mater.*, 2018, **10**, 102–113.
35 A. Rudola, D. Aurbach and P. Balaya, A new phenomenon in sodium batteries: Voltage step due to solvent interaction, *Electrochem. Commun.*, 2014, **46**, 56–59.
36 J. Guo, X. Wu, F. Wan, J. Wang, X. Zhang and R. Wang, A Superior $Na_3V_2(PO_4)_3$-Based Nanocomposite Enhanced by Both N-Doped Coating Carbon and Graphene as the Cathode for Sodium-Ion Batteries, *Chem. – Eur. J.*, 2015, **21**, 17371–17378.
37 K. Saravanan, C. W. Mason, A. Rudola, K. H. Wong and P. Balaya, The First Report on Excellent Cycling Stability and Superior Rate Capability of $Na_3V_2(PO_4)_3$ for Sodium Ion Batteries, *Adv. Energy Mater.*, 2013, **3**, 444–450.